

MATERIALS SCIENCE

Exploiting mammalian low-complexity domains for liquid-liquid phase separation–driven underwater adhesive coatings

Mengkui Cui^{1,2,3}, Xinyu Wang^{1,2,4}, Bolin An¹, Chen Zhang¹, Xinrui Gui^{2,5}, Ke Li¹, Yingfeng Li^{1,2,4}, Peng Ge⁶, Junhu Zhang⁶, Cong Liu⁵, Chao Zhong^{1*}

Many biological materials form via liquid-liquid phase separation (LLPS), followed by maturation into a solid-like state. Here, using a biologically inspired assembly mechanism designed to recapitulate these sequential assemblies, we develop ultrastrong underwater adhesives made from engineered proteins containing mammalian low-complexity (LC) domains. We show that LC domain–mediated LLPS and maturation substantially promotes the wetting, adsorption, priming, and formation of dense, uniform amyloid nanofiber coatings on diverse surfaces (e.g., Teflon), and even penetrating difficult-to-access locations such as the interiors of microfluidic devices. Notably, these coatings can be deposited on substrates over a broad range of pH values (3 to 11) and salt concentrations (up to 1 M NaCl) and exhibit strong underwater adhesion performance. Beyond demonstrating the utility of mammalian LC domains for driving LLPS in soft materials applications, our study illustrates a powerful example of how combining LLPS with subsequent maturation steps can be harnessed for engineering protein-based materials.

INTRODUCTION

Underwater adhesive systems in many marine organisms are known to form coacervates via liquid-liquid phase separation (LLPS). For example, the Sandcastle worm (*Phragmatopoma californica*) secretes an adhesive glue—a dense complex coacervate—with two oppositely charged polyelectrolyte adhesives (1), while marine mussel foot proteins (e.g., Mfp3S) confer adhesion by forming coacervates driven by inter- or intramolecular electrostatic interactions and hydrophobic interactions among the nonpolar residues (2, 3). The practical advantages of exploiting the ability of LLPS to generate condensed fluids are especially obvious for adhesive applications: They not only readily extend (spread) over the surface of wet mineral substrates due to low interfacial energy but also resist being dispersed in the surrounding seawater (2). Marine creatures thus have been the focus of bioinspired and biomimetic adhesive research efforts with LLPS-enabled adhesives variously harnessing coacervation based on electrostatic interactions between oppositely charged electrolytes (4–6) or on cation- π interactions (7–9). However, the formation and performance of marine organism–inspired LLPS-enabled adhesives are often dependent on solution pH and/or salt concentration, thus seriously limiting their practical applications (4, 5, 7, 9).

Beyond marine-inspired adhesives, there is an emerging awareness that intracellular LLPS may be a ubiquitous mechanism underlying the intracellular organization of biomolecular condensates in living cells (10–12). LLPS is known to facilitate functional compartmentalization and other cellular activities without the involvement of a membrane. For example, centrosomes (13), Balbiani bodies (14), and

nuclear amyloid bodies (15) achieve their normal (physiological) functions via LLPS, followed by liquid-to-solid maturation in mammalian cells. These hierarchical and sequential assemblies can provide order in nature, for example, by promoting the localized formation of gels even when the cytosolic concentration of a scaffolding protein is far below the critical gelation point (12). It is somewhat conspicuous then that despite a recent explosion in biological research about the contribution of LLPS-mediated processes to both human diseases and regulatory functions of mammalian proteins containing so-called low-complexity (LC) domains, these domains have not been explored in protein engineering approaches for functional adhesive coatings.

Given that many biological condensates involving LC domains form and function under physiological conditions, we hypothesize that the underlying assembly principle that drives the formation of biological condensates in cells (16–20) can be explored and potentially rationally integrated into the design of strong underwater adhesives. Pursuing this idea, we here searched through an inventory of LLPS-driven LC domains from humans and chose to work with an LC domain of the transactive response (TAR) DNA binding protein of 43 kDa (TDP43). We paired this domain with mussel foot protein 5 (Mfp5) to create TDP43 LC-Mfp5 (TLC-M) proteins and explore their coating formation over various substrates and their respective contributions to LLPS-enabled underwater adhesion. We observed a notable temperature-dependent phenomenon that ultimately improved our understanding of LC domain–mediated LLPS and allowed us to harness LLPS, followed by a liquid-to-solid maturation process to develop a new class of protein-based coating materials. Notably, the resultant protein coatings can be uniformly deposited on substrates even under very harsh solution conditions and exhibit strong underwater adhesion over a wide range of pH values and salt concentrations.

RESULTS

Design and sequential assemblies of TLC-M fusion protein

Seeking to develop strong underwater adhesives, we rationally selected TDP43 LC, which is the LC domain of the mammalian

Copyright © 2019 The Authors, some rights reserved; exclusive licensee American Association for the Advancement of Science. No claim to original U.S. Government Works. Distributed under a Creative Commons Attribution NonCommercial License 4.0 (CC BY-NC).

¹Materials and Physical Biology Division, School of Physical Science and Technology, ShanghaiTech University, Shanghai 201210, China. ²University of Chinese Academy of Sciences, Beijing 100049, China. ³Shanghai Institute of Organic Chemistry, Chinese Academy of Sciences, Shanghai 200032, China. ⁴Shanghai Institute of Ceramics, Chinese Academy of Sciences, Shanghai 200050, China. ⁵Interdisciplinary Research Center on Biology and Chemistry, Shanghai Institute of Organic Chemistry, Chinese Academy of Sciences, Shanghai 200032, China. ⁶State Key Laboratory of Supramolecular Structure and Materials, College of Chemistry, Jilin University, Changchun 130012, China. *Corresponding author. Email: zhongchao@shanghaitech.edu.cn

TDP43 (21) from an inventory of LLPS-driven LC domains (Fig. 1A). We also chose to work with Mfp5, a protein that is representative of 3,4-dihydroxyphenylalanine (DOPA)-containing mussel adhesive proteins originating from *Mytilus edulis* (Fig. 1B) (22). We constructed a genetic fusion construct, TLC-M, with an appended N-terminal histidine (His)-tag (to facilitate purification) using isothermal one-step Gibson DNA assembly (Fig. 1C). In our design, the LC domain of TDP43 is incorporated because fusion proteins containing this family of domains are known to undergo LLPS to form liquid-like condensates; followed by a liquid-to-solid phase transition, these condensates eventually mature into amyloid fibers (Fig. 1D) (17, 21). In particular, the α -helical component, known as the hydrophobic patch in the center (residues 320 to 340) of the LC domain, is believed to be responsible for TDP43 protein's self-assembly and LLPS (23, 24).

These LC domain-induced liquid-like condensates have several distinctive fluidic properties (e.g., the ability to fuse, flow, and undergo fission) (21, 25, 26) that may promote surface absorption and wetting (27), while nanofiber formation via a liquid-to-solid phase transition

contributes to enhanced cohesiveness (28–30). These complex processes closely recapitulate the dynamic assembly processes of sandcastle worm adhesives and barnacle cements (1, 31), during which the protein constituents are preassembled in an initial phase separation step and then undergo a curing step, resulting in a very efficient function by combining the wetting and adsorption properties on wet surfaces, interfacial adhesion, and cohesion. In addition, the TDP43 LC domain contains only one tyrosine residue; thus, subsequent posttranslational modification with tyrosinase—a necessary step to achieve improved adhesion for mussel foot proteins—would not disrupt the self-assembly of the modified fusion protein. Last but not least, we predicted that the TLC-M nanofiber coatings formed via these sequential assemblies would exhibit very strong underwater adhesion owing to their large surface area and the adhesive residues present on the Mfp5 domains, which would be exposed at the surface of the nanofibers, external to the amyloid core.

In our initial attempts to apply self-assembled TLC-M as adhesive coatings, we observed a notable temperature-dependent phenomenon. Specifically, when incubated at 4°C, the fusion protein TLC-M formed

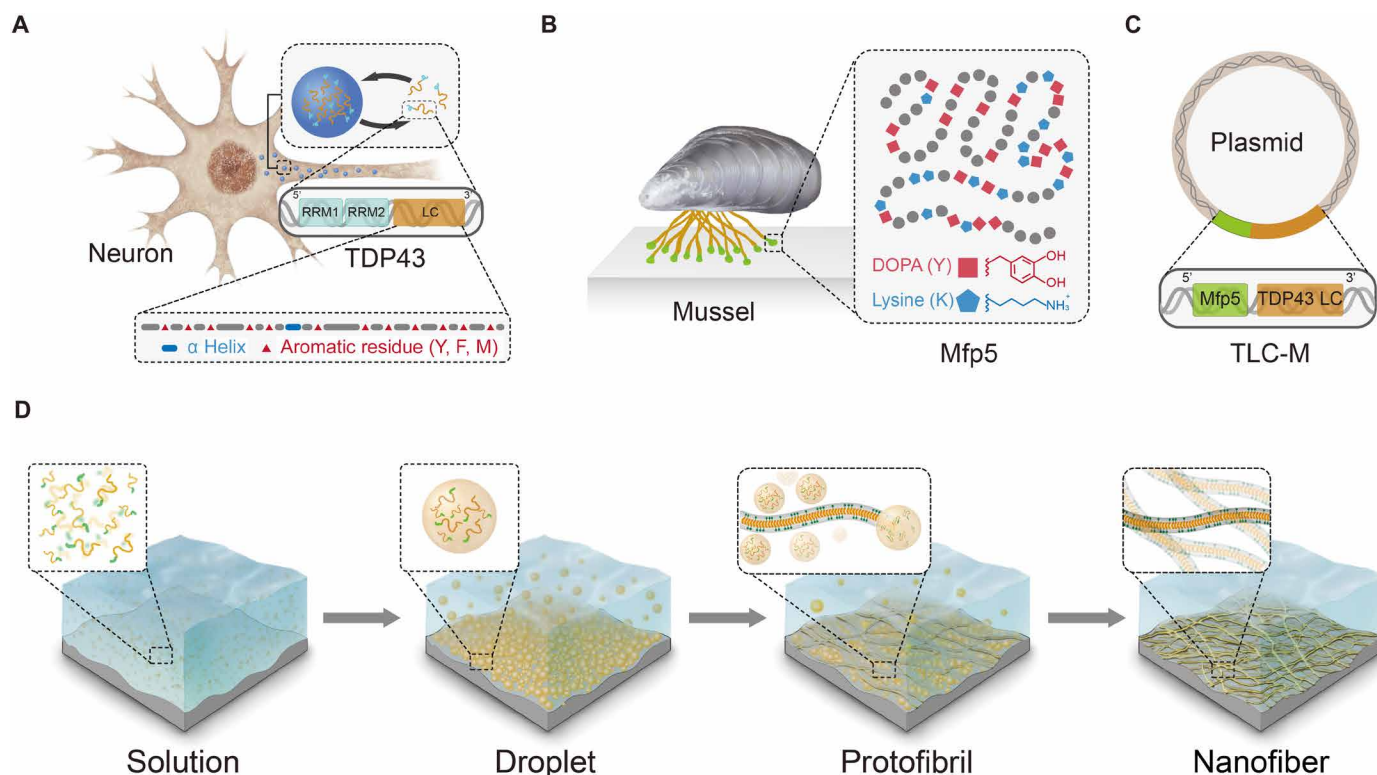


Fig. 1. Engineering mammalian LC domains for protein-based strong underwater adhesives through LLPS, followed by maturation into nanofibers. (A) Schematic of TDP43, a human DNA binding protein, which, along with specific RNAs, forms TDP43 ribonucleoprotein granules that mediate cellular processes in neuron cells. TDP43 contains both RNA recognition motifs (RRMs) and a LC domain, which is an intrinsically disordered domain enriched in glycine and uncharged polar amino acid residues. The LC domain contributes to the self-assembly of ribonucleoprotein granules, which is driven by a process termed LLPS. The featured α helix domain and aromatic residues in TDP43 LC sequence are highlighted below. (B) Schematic of the adhesive protein Mfp5 that functions in the adhesion plaques of marine mussels. Mfp5, a mussel adhesion foot protein rich in lysine and DOPA residues, displays a random coil structure in solution and is essential for the interfacial underwater adhesion of mussels. (C) The modular genetic design of adhesive proteins is enabled by rationally fusing sequences encoding the protein domains shown in (A) and (B) to form a His-tagged TLC-M fusion protein. (D) TLC-M fusion protein monomers in solution can assemble into condensed liquid-like droplets driven by LLPS (left). The liquid-like droplets tend to spread over and adsorb on surfaces, facilitating a priming process for the TLC-M coating (middle left). In a follow-up maturation process, the liquid-like droplets are locally enriched near the substrate surface. These droplets have high concentrations of protein monomers, thus promoting the formation of protofibrils on the substrate (middle right). Additional monomers can then aggregate on these surface-localized protofibrils, eventually forming amyloid nanofiber coatings on the surface. The TLC-M nanofiber coatings exhibit strong underwater adhesion owing to their large surface area and the adhesive properties of the Mfp5 domains, which are exposed at the surface of the nanofibers, external to the amyloid core.

a dense and uniform coating on a glass substrate (Fig. 2A, top left). In contrast, when incubated at 25°C, only very sparse and heterogeneous depositions were formed on a glass slide (Fig. 2A, bottom left). Furthermore, staining with the amyloid-specific dye Congo red (CR) revealed intense and uniform signals for the TLC-M coating formed at 4°C (Fig. 2A, top left, and fig. S1), whereas the coating formed at 25°C had a much weaker staining signal (Fig. 2A, bottom left).

To further confirm the amyloid nature of the coatings, we performed x-ray fiber diffraction. The coating materials exhibit a typical

cross- β diffraction pattern, which is the signature of amyloid fiber (Fig. 2A, top right) (32, 33). Moreover, the x-ray fiber diffraction pattern of TLC-M nanofibers is close to that of TDP43 LC nanofibers (fig. S4A), suggesting that fusion of the Mfp5 protein into TDP43 LC did not disrupt the self-assembly of TDP43 LC. Transmission electron microscopy (TEM) and atomic force microscopy (AFM) analyses confirmed that the TLC-M coating materials formed at 4°C were nanofiber mesh structures composed of hierarchically arranged nanofibers (Fig. 2B). Note that although the depositions formed at

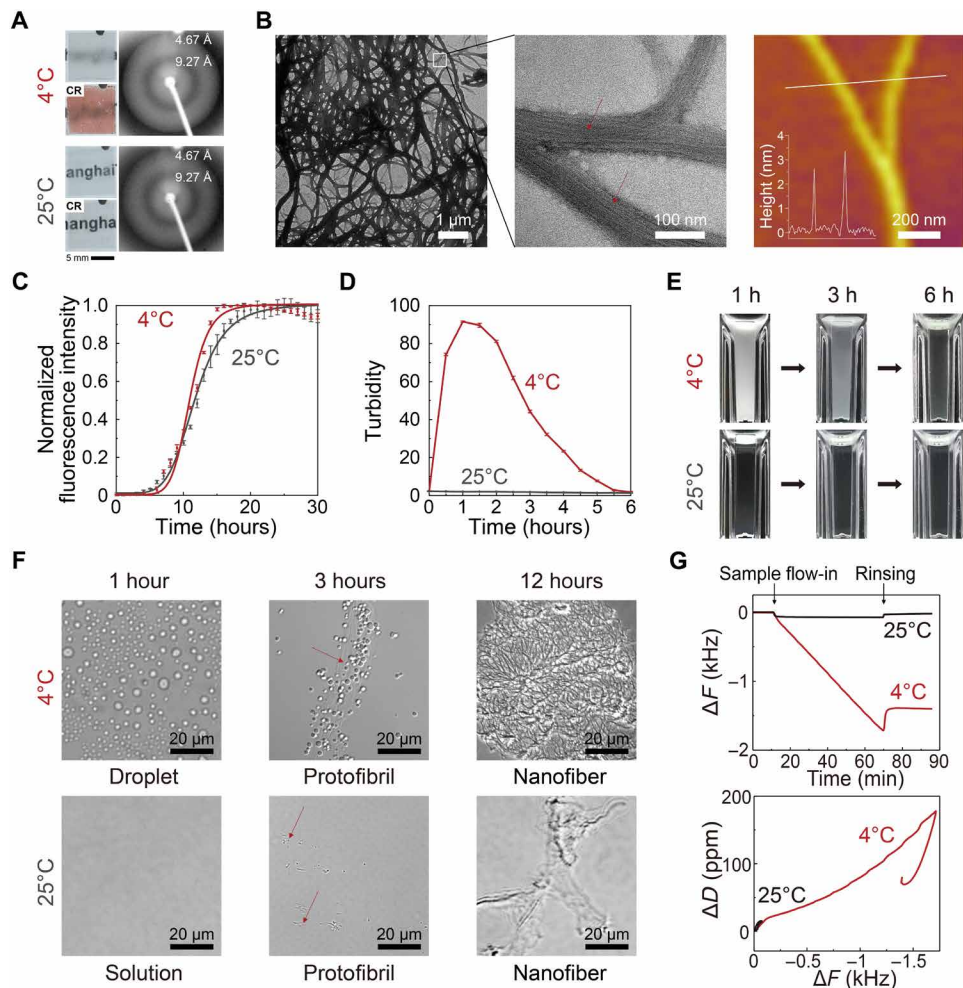


Fig. 2. Morphological and structural characterization of LLPS-induced TLC-M adhesive coatings. (A) Photographs of adhesive coatings (top left) produced by incubating TLC-M monomer solutions at 4 and 25°C and staining of the corresponding samples with CR (lower left). X-ray fiber diffraction pattern (right) of TLC-M nanofibers of two samples showed a typical diffraction pattern of cross- β spine of amyloid nanofibers in which the meridional reflection is ~ 4.67 Å (corresponding to the spacing between β strands within each layer of β sheets in the fibril) and the equatorial reflection is ~ 9.27 Å (corresponding to the intersheet packing distances between each layer of β sheets in the fibril). (B) Morphological characterization of the hierarchical structure of TLC-M coatings formed at 4°C. TLC-M coatings were dense nanofiber meshes [transmission electron microscopy (TEM) image; left] formed from nanofiber bundles that assembled via the lateral stacking of amyloid nanofibers (TEM image; middle). These nanofibers are about 3 nm in diameter [atomic force microscopy (AFM) image; right]. (C) Thioflavin T (ThT) fluorescence curve of TLC-M in solutions (2 mg/ml) incubated at 4 and 25°C. A ThT fluorescence assay was applied to monitor and quantify the kinetics of amyloid nanofiber formation. (D) Turbidity-time curve of TLC-M in solution (1 mg/ml) incubated at 4 and 25°C, measured at optical density at 600 nm (OD_{600}). (E) Photographs of TLC-M solutions (1 mg/ml) incubated at 4 and 25°C taken at different time intervals. (F) Differential interference contrast (DIC) microscopy images of phase separation-induced assembly of TLC-M protein monomers adsorbed on a glass surface at 4 and 25°C assessed after 1, 3, and 12 hours of incubation. LLPS-driven formation of liquid-like droplets happens during the first 6 hours, followed by the appearance of protofibrils in the vicinity of the liquid-like droplets. TLC-M monomers then aggregate on the protofibrils, eventually producing dense TLC-M nanofiber coatings. (G) Frequency change comparison in quartz crystal microbalance with dissipation (QCM-D) experiments showing the different adsorption capacities of TLC-M solutions (1 mg/ml) to a gold surface at 4 and 25°C (top). Plots of ΔD versus ΔF (bottom) corresponding to the curve shown at the top. The $\Delta D/\Delta F$ value indicates the stiffness of the coatings: Higher $\Delta D/\Delta F$ values suggest softer materials. ThT and turbidity data show means \pm standard error of the mean (s.e.m.) of three replicate samples. ppm, parts per million.

25°C were very sparse, x-ray fiber diffraction, TEM, and AFM revealed that these materials were also assembled as amyloid nanofibers (Fig. 2A, bottom right, and fig. S2, A and B).

Intrigued by the observation that incubation of TLC-M monomers at 25°C produced amyloid nanofibers but formed only sparse depositions on the glass substrate, we conducted a thioflavin T (ThT) kinetics assay to monitor the amyloid assembly process over time at low (4°C) and high (25°C) temperatures (Fig. 2C and figs. S3C and S4B). The results revealed the following: (i) Whereas the high-temperature samples exhibited amyloid assembly that started soon after the start of incubation, the low-temperature samples had a much longer lag time before initiating amyloid assembly. (ii) It took about 25 hours for the TLC-M monomers of the high-temperature samples to complete their assembly into amyloid nanofibers. In contrast, the amyloid assembly process for low-temperature samples was completed within a much shorter time window (~10 hours). (iii) Higher concentration of TLC-M proteins led to a relatively shorter lag phase and shorter time to reach stationary phase, implying faster amyloid nanofiber formation kinetics for solution with higher protein concentration, independent of solution temperature.

LLPS behaviors and surface adsorption capacities of TLC-M fusion protein

The extreme differences that we observed in the thickness and uniformity of coverage of the coatings formed at low versus high temperature and our findings that the temperature difference altered, but did not prevent, the amyloid assembly of TLC-M monomers collectively suggest a kinetically trapped state in the low-temperature samples during which TLC-M monomers form liquid-like condensates in a process driven by LLPS. A hallmark feature of LLPS is the high turbidity of solutions. We conducted turbidimetry based on optical density measurements at 600 nm (OD_{600}) for purified TLC-M monomer solutions over a 6-hour incubation at 4 and 25°C and observed that whereas the turbidity of the 4°C samples rose from a very low level, subsequently rose sharply to quickly reach a plateau that lasted for around 2 hours, and then gradually declined, that of the 25°C samples rose slightly but then sharply decreased without exhibiting any plateau (Fig. 2D and fig. S4C). We hypothesized that the 2-hour turbidity plateau of the 4°C samples corresponds to the aforementioned kinetically trapped state during which the liquid-like condensates are equilibratedly formed. Notably, higher protein concentrations seemed to promote faster formation of liquid-like condensates in solution, as indicated by the steeper slope of the curves representative of higher concentrations (fig. S3A).

Subsequent macro- and microscale observations of the low- and high-temperature samples collected at different time points further supported this hypothesis. Photographs of the low-temperature TLC-M incubation process showed that the low-temperature sample solutions became cloudy within several minutes, remained cloudy for 4 to 5 hours, and then became clear after 6 hours (Fig. 2E), by which time the amyloid nanofiber assembly process has already begun. Consistently, differential interference contrast (DIC) microscopy and TEM images (Fig. 2F and fig. S2C) showed that liquid-like droplets formed in the low-temperature TLC-M samples within 1 hour, whereas no droplets formed at any point for the high-temperature TLC-M samples. In the period of time between the initial deposition of these liquid-like droplets and eventual amyloid nanofiber formation in the low-temperature TLC-M samples, we observed that intermediate “protofibrils” formed in the immediate vicinity of the initially adsorbed

liquid-like droplets. When the LC domain-mediated LLPS process was monitored for solution turbidity under a variety of experimental conditions, it was seen that temperature, ionic strength, and solution pH all affected the LLPS-driven formation of liquid-like droplets but temperature appeared to exert the largest influence (fig. S5). More specifically, lower temperature, lower ionic strength, and higher pH values all promoted phase separation of the TLC-M monomers.

We next applied quartz crystal microbalance with dissipation (QCM-D) experiments to examine the different adsorption capacities (34) of TLC-M on a gold surface at 4 and 25°C (Fig. 2G and fig. S6). The adsorption capacity of the TLC-M solution at low temperature was substantially higher than that of high temperature. Moreover, the large value of the acoustic ratio ($\Delta D/\Delta F$) observed for the low-temperature solution was indicative of the presence of soft materials adsorbed on the gold surface. In addition, the QCM-D results revealed that higher protein concentration promoted faster settling and thus adsorption of the liquid-like droplets on the gold surface (fig. S3B). Previous studies suggest that gravity plays a role in promoting surface adsorption of liquid-like condensates toward a given substrate (2). To confirm this hypothesis, we applied a bicinchoninic acid (BCA) assay to quantify and compare the amount of liquid-like droplets adsorbed on an upper surface (a glass slide floating on a solution surface) and a bottom surface (a glass slide sitting at the bottom of a solution). The results based on five independent samples showed that more protein coatings formed at the bottom surface than the upper surface after 1 hour of incubation with a mass adsorption ratio of ~0.3 for the upper to bottom surface (table S1). We thus conclude that liquid-like droplets are able to adsorb on both upper and bottom surfaces but gravity plays a notable role in promoting droplet settlement on a substrate.

Collectively, these results highlight the prominent role of LLPS-driven liquid-like condensates in the formation of dense and uniform amyloid nanofiber coatings at substrate surfaces at a low temperature: Compared with nonphase-separated solution proteins, these liquid-like condensates have much lower interfacial energy that enable droplets to effectively spread over gold surface (the so-called wetting properties). Conceivably, hydrophobic interactions along with π - π interactions between the proteins themselves can also drive the continuous stacking of protein on top of the former protein layer adsorbed to the gold surface (2, 5).

Underwater adhesion performance of TLC-M coatings

To directly measure the underwater adhesion performance of TLC-Ms, we used colloidal probe technique based on AFM that assesses the asymmetric adhesion of nanomaterials that initially bind to clean and smooth mica in an aqueous buffer at room temperature (25°C) (Fig. 3A and fig. S7C) (29). We initially examined how the differences in coating density and uniformity between the low temperature- and high temperature-induced TLC-M coatings affected adhesion performance. The low temperature-induced TLC-M coatings exhibited markedly and significantly stronger adhesion than the high-temperature coatings (Fig. 3B). The adhesion performance of the low-temperature coating was very close to the value reported for the strongest-to-date amyloid protein-based underwater adhesive (underwater adhesion energy, 18.1 mJ/m²). This huge difference in adhesion underscores the powerful contribution of the LLPS-driven process in promoting both the initial priming and wetting of a substrate and the subsequent self-assembly of the locally concentrated TLC-M monomers into extremely dense and highly uniform amyloid nanofibers.

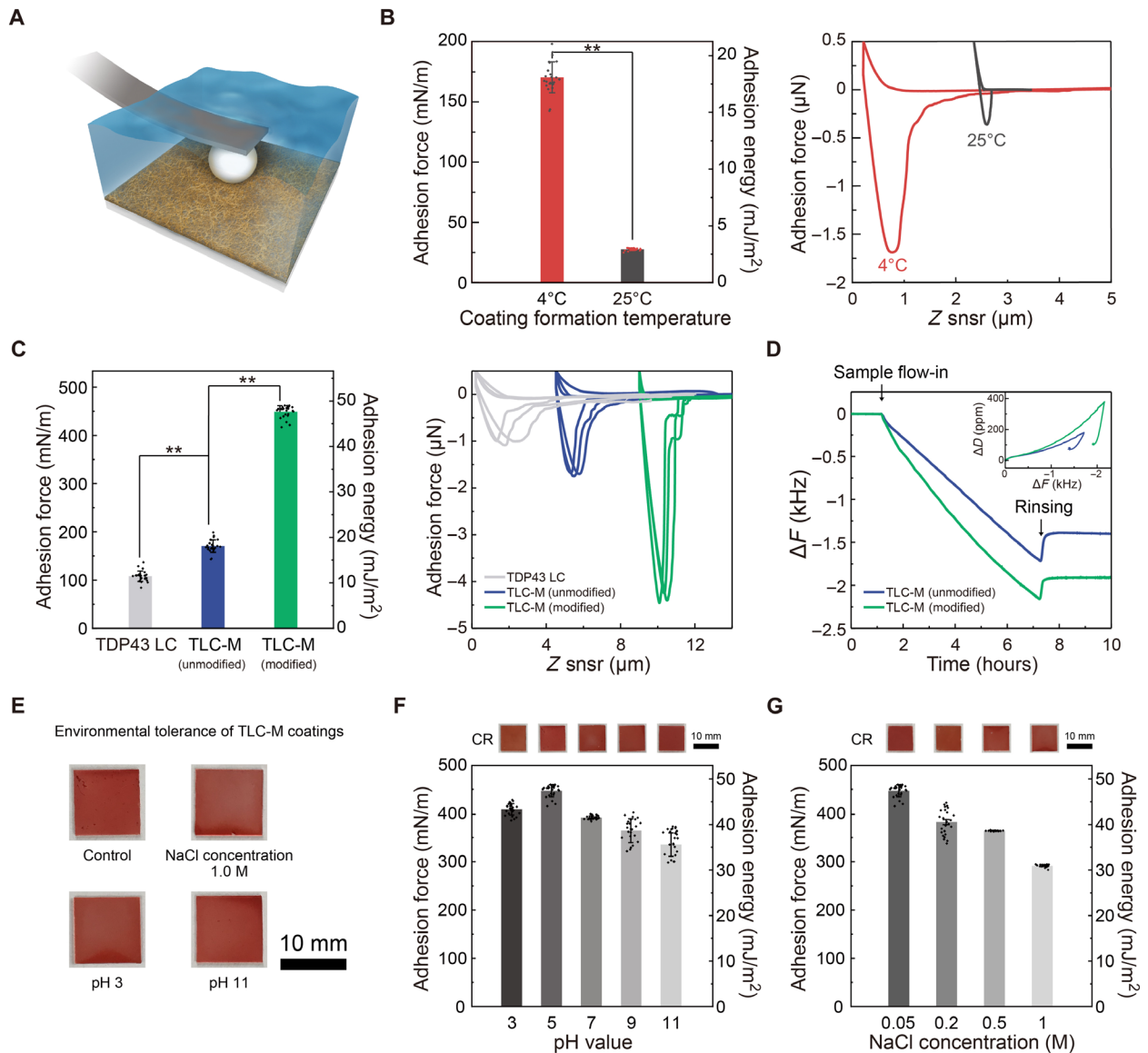


Fig. 3. Underwater adhesion performance of adhesive coatings made of mammalian LC domain proteins. (A) Schematic of a colloidal AFM probe used to measure the asymmetric adhesion of adhesive coatings on smooth mica surfaces. (B) Comparison of adhesion forces [normalized force (F/R) and adhesion energies ($E_{ad} = F/3\pi R$)] for TLC-M coatings produced at 4 and 25°C (measured with a gold probe tip). Representative adhesion force-distance curves in the right panel were collected on one spot of the coated mica surface using the single force mode (gold probe tip). (C) Comparison of adhesion forces and adhesion energies for the TDP43 LC domain (control), unmodified TLC-M, and DOPA-modified TLC-M coatings produced at 4°C (gold probe tip) (left) and representative adhesion force-distance curves of the control TDP43 LC, unmodified TLC-M, and DOPA-modified TLC-M coatings (right); the curves correspond to three random spots of the coated mica surface (single force mode; gold probe tip). (D) Frequency change comparison in QCM-D experiments showing the different adsorption capacities of unmodified TLC-M and DOPA-modified TLC-M coatings for a gold surface at 4°C. Inset: Plots of ΔD versus ΔF corresponding to the frequency change curve. (E) CR staining of DOPA-modified TLC-M coatings (produced in solution pH 5, 0.05 M NaCl) after a continuous 7-day incubation under harsh conditions (pH 3 and 11 buffers, 1.0 M high NaCl concentration buffer). (F) Adhesion forces and adhesion energies for DOPA-modified TLC-M coatings produced at a range of pH values (3 to 11) at 4°C measured in pH 5 buffer with a gold probe tip. (G) Adhesion forces and adhesion energies for DOPA-modified TLC-M coatings produced at a range of NaCl concentrations (50 to 1000 mM) at 4°C measured in pH 5 buffer with a gold probe tip. $**P < 0.01$, Student's t test. Error bars indicate the SD. For each comparison in (B), (C), (E), and (F), $n = 25$ (five spots per mica plate, with each spot sampled five times using single force mode). In (B) and (D), the adhesion force curves are plotted as force-displacement curves: The x axis labeled as Z snsr (Z sensor) represents the displacement between the sample surface and the resting position of the cantilever (rather than the actual distance between the sample surface and the AFM tip). Note that all the underwater adhesion measurements were performed at 25°C aqueous temperature.

As the TLC-M fusion monomers also contain a marine mussel adhesive protein, we next assessed how the presence of the Mfp5 fusion domain would influence the adhesion of three different coatings by coating mica at low temperature with the TDP43 LC domain

only, unmodified TLC-M, or tyrosinase-modified TLC-M bearing DOPA residues (Fig. 3C). Even lacking tyrosinase treatment, the presence of the Mfp5 fusion domain substantially increased the adhesive strength of the coating: The adhesion of the unmodified

TLC-M coating was 1.6 times stronger than the coating made from the TDP43 LC domain alone. The *in vitro* conversion of the tyrosine residues on the TLC-M monomers into DOPA residues via tyrosinase treatment increased the adhesive strength of the amyloid nanofiber coating by more than 2.7 times with underwater adhesion energy approaching 48.1 mJ/m² [versus 20.9 mJ/m² in previously reported amyloid underwater adhesives (29)], a very impressive adhesion performance for a protein-based underwater adhesive (Fig. 3C). The TLC-M coatings had very similar adhesion properties when measured at different solution temperatures (fig. S7, A and B), suggesting that the adhesion performance of TLC-M coatings are independent of temperature (although their formation is sensitive to solution temperature). In addition, beyond their contribution to increasing adhesion, it was also clear that the DOPA residues on the Mfp5 fusion domains enhanced intramolecular interactions and absorption onto the gold substrate during LLPS-mediated deposition: QCM-D analysis showed that the tyrosine-modified TLC-M coatings were even denser than the unmodified TLC-M coatings (Fig. 3D). Notably, these coatings exhibited outstanding environmental tolerance: They showed no obvious deterioration or loss (as revealed by CR staining) even after incubation under their respective harsh condition solutions for 7 days (Fig. 3E).

There are important distinctions between LC domain-driven LLPS and coacervation, which is another LLPS mechanism that is used by sandcastle worms for priming and wetting and that has inspired existing biomimetic adhesives (1). Phase transition from liquid-like droplets to nanofibers was not found for LLPS in sandcastle worms. In addition, formation of those coacervate structures is mainly electrostatic driven (35) and is thus dependent on pH, and these engineered oppositely charged coacervates are therefore currently limited to applications in narrow pH ranges (5). In addition, cation- π interactions inspired by mussel foot protein can also mediate coacervate formation, yet the application of adhesives based on this type of coacervate has been seriously limited—especially in high-concentration salt solutions—by the known strong influence of solution ionic strength on adhesion performance (7–9).

Given these known limitations of previous coacervate-based adhesives under extreme conditions and in light of reports from the biochemistry literature about the major driving forces of hydrophobic α helices and aromatic residues of the TDP43 LC domains for LLPS-promoting functions (distinct from the electrostatic and cation- π interactions) (24), we speculated that TDP43 LC domain-mediated LLPS may enable coating applications over a wide range of solution pH values and ionic strengths. We were able to deposit thick and uniform TLC-M coatings over a wide range of pH values (pH 3 to 11) at 4°C (Fig. 3F) and NaCl concentrations (0.05, 0.2, 0.5, and 1.0 M) (Fig. 3G). When we used AFM colloidal probes to measure the adhesive strength of the TLC-M coatings produced under these harsh conditions, we found that the resultant TLC-M coatings maintained similar levels of performance compared to coatings formed at pH 5 and 50 μ M NaCl conditions, although the slight decreases we observed with increasing pH values and NaCl concentrations are notable (Fig. 3, F and G). These results thus suggest that salt concentration has a more pronounced impact than does pH on adhesion performance. Given the known fact that high pH causes oxidation of DOPA residues, we can infer that DOPA residues are contributing a relatively minor proportion of the adhesive strength of the TLC-M coatings deposited at high pH.

TLC-M adhesive coating applications

As it is likely that the hydrophobic α helix and aromatic residues in the LC domain (24) drive the LLPS that we observed during low-temperature TLC-M coating deposition, we next undertook the challenge of applying TLC-M coatings to polytetrafluoroethylene (PTFE; “Teflon”), which is an extraordinarily “nonstick” substance. Following incubation of flat Teflon wafers overnight at 4°C, comparison of ultraviolet (UV) light (254 nm) images and scanning electron microscopy (SEM) images revealed the deposition of a thick and uniform TLC-M coating on the Teflon (Fig. 4A, top, and fig. S8A), and water contact angle analysis demonstrated that this coating significantly and markedly decreased the contact angle of the hydrophobic PTFE surface from 108.4° \pm 1.4° to 68.7° \pm 2.1° (Fig. 4A, top).

When we incubated uncoated and TLC-M-coated PTFE wafers with CdSeS@ZnS quantum dots (QDs), which can interact with the TLC-M molecules via His-tag affinity, we observed that QDs were uniformly adsorbed on the surface of the coated Teflon wafers but found that almost no QDs were present on uncoated Teflon (Fig. 4A, bottom). A cross-section image of the TLC-M coating by SEM revealed that the surface of the Teflon wafer had a thick and uniform coating (Fig. 4B, top). X-ray photoelectron spectroscopy (XPS) spectral analysis revealed that, compared to uncoated Teflon, a Teflon wafer coated with TLC-M amyloid nanofibers had almost no signal for fluorine (F 1s) but had clear signals for oxygen (O 1s) and nitrogen (N 1s) from the protein coating layers (Fig. 4B, bottom). We also found that coated wafers had decreased signals for carbon (C 1s) arising from C–F bonds but had increased signals for carbon (C 1s) arising from C–O, C–N, and C–C bonds.

Exploiting the ability of our LLPS-driven TLC-M process to coat difficult-to-access surfaces, we also conducted proof-of-concept demonstrations for the coating of difficult-to-access interior surfaces including the interior surfaces of a flexible Teflon pipe and the channel of a microfluidic device (Fig. 4, C and D). Again, the ability of the TLC-M coatings to adsorb QDs allowed us to posttreat and thus visualize TLC-M coatings on these and other challenging substrates [e.g., highly flexible polyethylene terephthalate (“Mylar”) thin films], and the successful formation of thick and uniform TLC-M coatings on each of these materials underscored that our LLPS-driven technique can be used to coat a great diversity of surfaces (fig. S8, B and C). Note that gravity plays a role in promoting the adsorption of liquid-like condensates and thus the possible formation of thicker coatings on the bottom side of the interior surfaces. However, no obvious differences of fluorescence strength were actually observed on the upper and bottom surfaces of the microfluidic devices and the Teflon pipe. We ascribe this observation to the specific binding of QDs only onto the outer layer of the coatings—with QD treatment after coating formation, the fluorescence strength of QDs is thus proportional to the specific surface area rather than the thickness of the coatings.

To further explore practical applications of the LLPS-driven TLC-M adhesives, we also used these materials as underwater glues for repairing damage. We coinjected purified TLC-M monomers in solution with nonsticky polystyrene (PS) microspheres into a damaged site scratched onto a PTFE substrate (Fig. 4E). Upon incubation at 4°C for 12 hours, an LLPS-driven TLC-M coating formed on the surface of the damage site and the microspheres; the coating functioned as a glue to cluster the microspheres to each other and to the substrate surface, thereby retaining them in place and filling the damage site even under aqueous condition. Both fluorescence and SEM images showed that the microspheres specifically accumulated

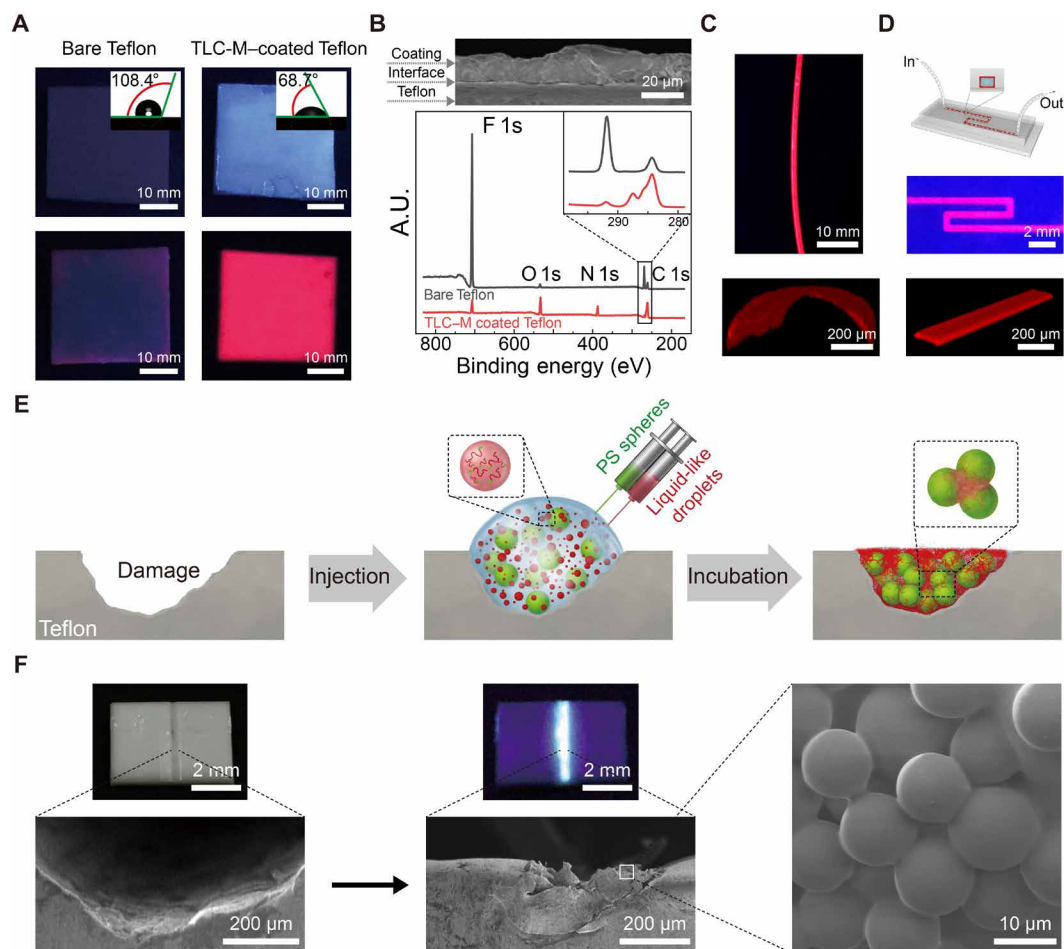


Fig. 4. Applications of LLPS-induced TLC-M adhesive coatings. (A) Digital camera images were taken under 250-nm UV light for uncoated (left) and TLC-M-coated Teflon substrates (right). The inset was water contact angle analysis, and the bottom was red quantum dot (QD) adsorption on corresponding substrates. (B) SEM sectional image of a continuous layer of LLPS-induced TLC-M adhesive coating formed on Teflon (top) and corresponding x-ray photoelectron spectroscopy (XPS) showing the distinctive element signals representative of N, O, and C (from protein structures) in the coated Teflon substrate, in contrast with the dominant F and C signals shown in the bare Teflon. A.U., arbitrary unit. (C) UV-illuminated photograph (top) and three-dimensional (3D) confocal micrograph (bottom) of a Teflon pipe showing red QDs adsorbed on the interior walls of the TLC-M-coated pipe. (D) Schematic (top), UV-illuminated photograph (middle), and 3D confocal micrograph (bottom) of a microfluidic device with a TLC-M-coated channel that was posttreated with red QDs. (E) Schematic illustration showing the repair of damage (scratch) on a Teflon substrate. We coinjected purified TLC-M monomers in solution with nonsticky fluorescent spherical PS microspheres around the damage site. Upon incubation at 4°C for 12 hours, an LLPS-induced TLC-M coating formed on the substrate and on the surface of the PS microspheres, acting as a glue that aggregated the microspheres to each other and with the substrate surface, thereby retaining them in place and filling the damage site (right). (F) Photograph (top) and SEM (bottom) images showing the damaged Teflon substrates before and after repair made using LLPS-induced coatings. Photograph of the repaired sample is taken under UV light (254 nm). A zoomed-in SEM image shows that the microspheres were piled up and glued together in the damage site.

in the damage site (Fig. 4F, middle and right), demonstrating the potential of the LLPS-driven coating for damage repair.

DISCUSSION

Our engineering demonstration of the exploitation of LC domain-mediated LLPS and maturation in developing ultrastrong underwater adhesive coatings is the first of many potentially great materials and bioengineering applications that could be enabled or improved by a better understanding of how mammalian or other LC domains affect the nonequilibrium characteristics of the phase behavior of proteins. As demonstrated, the designed mammalian LC domain-containing protein TLC-M exhibits intrinsic advantages as a new type of adhesive coating material. TLC-M also benefits from the temporal specification

of functions resulting from its hierarchical and sequential assembly: The LLPS process enables surface wetting and adsorption, while liquid-to-solid maturation promotes amyloid nanofiber formation for strong adhesion. One can imagine other practical applications that could benefit from exploiting LC domain-mediated LLPS to precisely manipulate self-sustaining aggregation, assembly kinetics, or even dynamically arrested metastable products and phases. For example, bonding-on-demand protein-based cements can be created by kinetically controlling the assembly and disassembly of adhesive coatings, and membraneless microreactors that can facilitate specific activation of biosynthetic cascades can also be designed if appropriate enzymes are selectively trapped in the condensates.

Many important functional consequences of LLPS in cells have been described recently (36, 37). LLPS is known to function in

multifaceted roles, which may include facilitated metabolic reactions, sequestration of specific signaling factors, and the control of both the morphology and functions of intracellular structures (37–39). In addition, recent discoveries have shown that barnacle cement fibrils consist of proteins rich in conserved LC domains, which may contribute to the initial formation of a phase-separating fluid before cement deposition (31). Our work therefore opens the door for design thinking in bioengineering and materials engineering to incorporate LC domain sequences for phase transition–related molecular and cellular phenomena to help address fundamental questions in life science, medicine, and materials science. Additional studies similar to ours that use LC domains for engineering applications can continue to reveal the precise physical basis of how LC domains promote or attenuate LLPS. Moreover, if we can determine principles for designing molecular materials that allow the fine tuning of the behaviors of LC domain–containing proteins (16, 40), then we should be able to develop innovative new materials and biotechnologies that can perhaps even be introduced back into cells to allow researchers ever more precise control of cellular metabolism, structure, and physiology.

MATERIALS AND METHODS

Plasmids construction

The original pHis-parallel1 vector is a gift from S. L. McKnight's research group at the Department of Biochemistry, University of Texas Southwestern Medical Center. The pHis-parallel1 vector contains two 6× His at both ends of the open reading frame. The *TDP43 LC* and *Mfp5* genes were separately synthesized by GENEWIZ (Suzhou) and then amplified by polymerase chain reaction (PCR) with appropriate overhangs for Gibson assembly. *TDP43 LC* or recombinant gene *TLC-M* containing *TDP43 LC* and *Mfp5* was cloned into pHis-parallel1 vectors using one-step isothermal Gibson assembly. The cleaved vector and corresponding PCR products were mixed together with the Gibson Assembly Master 2× Mix (New England BioLabs) at 50°C for 1 hour and then transformed into DH5α *Escherichia coli* competent cells. PCR amplifications were carried out with primer oligos purchased from GENEWIZ. A Bio-Rad S1000 thermal cycler with dual 48/48 fast reaction modules (Bio-Rad) was used to perform PCR, ligations, and Gibson assembly. Gel extractions were carried out with QIAquick Gel Extraction Kits (QIAGEN). All constructs were sequence-verified by GENEWIZ.

Protein expression, purification, and tyrosinase modification

The recombinant plasmids containing *TDP43 LC* and *TLC-M* genes were transformed in BL21 (DE3) *E. coli* competent cells individually. The expression and purification of these proteins were carried out following protocol provided by S. L. McKnight's research group (21, 25). Specifically, the strains were grown to OD₆₀₀ of ~1.0 in 1 liter of LB containing carbenicillin (50 mg/ml) at 37°C. Protein expression was induced with 0.5 mM isopropyl-β-D-thiogalactopyranoside at 16°C overnight. Cells were collected by centrifugation at 5000g for 10 min, and the collected cell pellets were stored at –80°C. Five grams of the collected cell pellets were resuspended with 50 ml of tris-HCl buffer [50 mM tris-HCl and 500 mM NaCl (pH 7)]. Lysozyme (with a final concentration of 0.2 mg/ml) and 0.1 mM phenylmethylsulfonyl fluoride were also added in the solution to inhibit protein degradation by enzymes. Lysates were then incubated on ice for 30 min, followed by sonication for 30 min by a sonic dismembrator

(Fisherbrand Model 120). The insoluble portions of the lysates were removed through centrifugation at 20,000g for 30 min, and the separated supernatants were incubated with 2 ml of Ni–nitrilotriacetic acid (NTA) resin (Clontech) for 1 hour at room temperature. Beads that bound with TDP43 LC or TLC-M were collected by centrifugation at 300g for 5 min and washed with 50 ml of tris-HCl buffer [50 mM tris-HCl and 500 mM NaCl (pH 7)]. The mixed solutions were then loaded into 12-ml affinity columns (Sangon Biotech). Then, 100 ml of washing buffer [50 mM tris-HCl, 500 mM NaCl, and 40 mM imidazole (pH 7)] was passed through the columns to remove contaminated proteins with five consecutive washing steps before tyrosinase modification.

In vitro posttranslational modification by tyrosinase from mushroom (ST382401, Sigma-Aldrich) was carried out by following a previously reported protocol. (29) Specifically, the columns were firstly washed with 20 ml of tris-HCl buffer [50 mM tris-HCl and 500 mM NaCl (pH 7)] for two consecutive washing steps, 5 ml of mushroom tyrosinase solution [0.5 mg/ml; 20 mM sodium borate, 100 mM phosphate-buffered saline (PBS), and 100 mM ascorbic acid (pH 7.0)] was then added to columns containing protein-bound beads, and the resulting solutions were shaken for 2 hours at room temperature. Last, after washing twice with 20 ml of tris-HCl buffer [50 mM tris-HCl and 500 mM NaCl (pH 7)] to remove tyrosinase, modified proteins were eluted from the column via 5 ml of elution buffer [50 mM tris-HCl, 500 mM NaCl, and 500 mM imidazole (pH 7)] applied in five consecutive steps. The purified proteins were concentrated using Ultra-15 10K Centrifugal Filter Devices (Millipore, USA), and the concentrations were determined by absorbance at OD₂₈₀. The purity of purified proteins was confirmed with SDS–polyacrylamide gel electrophoresis. Samples were stored at 4°C for later use.

To compare tyrosinase-modified and tyrosinase-unmodified proteins, we also purified proteins without tyrosinase treatment. In this case, the in vitro posttranslational modification steps described above were not applied in the corresponding protein purification procedures.

Preparation of LLPS-induced liquid-like droplets and self-assembled amyloid nanofibers

Purified proteins in elution buffer [50 mM tris-HCl, 500 mM NaCl, and 500 mM imidazole (pH 7)] were concentrated to a final mass concentration of 1 mg/ml, the protein solutions were quickly cooled down and stored at 4°C, and cloudy solutions containing liquid-like droplets driven by LLPS gradually formed within 1 hour and were collected for detailed characterization. Data are presented in Fig. 2F and fig. S2C. Self-assembled amyloid nanofibers were obtained in protein solutions incubated at both 4 and 25°C overnight after purification. Data are presented in Fig. 2B and fig. S2 (A and B).

Important parameters that influence the formation of TLC-M liquid-like droplets

We tested several parameters that might affect the formation of liquid-like droplets during LLPS process, including protein concentration, storage temperature, ionic strength, and pH value. All the experiments were carried out immediately after protein purification, and the formation of liquid-like droplets in protein solutions was monitored on the basis of turbidity measurement. To test the influence of protein concentration on the formation of liquid-like droplets, we applied fresh purified TLC-M solutions with varied concentrations (0.2, 0.5, 1, and 2 mg/ml) incubated at 4 and 25°C to measure the turbidity over time.

Further, to test the influence of temperature on the formation of liquid-like droplets, we measured and compared the turbidity of TLC-M solutions (1 mg/ml) after dialyzing in dialysate buffers [20 mM tris-HCl, 50 mM NaCl, and 0.5 mM EDTA (pH 5)] at 4, 16, and 25°C for 1 hour. To assess the influence of ionic strength (varied NaCl concentration) on the formation of liquid-like droplets, we measured and compared the turbidity of TLC-M solutions (1 mg/ml) after dialyzing in dialysate buffers [20 mM tris-HCl and 0.5 mM EDTA (pH 5)] containing different NaCl concentrations (0.05, 0.2, 0.5, and 1.0 M) for 1 hour. To assess the influence of solution pH, we measured and compared the turbidity of TLC-M solutions (1 mg/ml) after dialyzing in dialysate buffers (20 mM tris-HCl, 50 mM NaCl, and 0.5 mM EDTA) at different pH values (3, 5, 7, 9, and 11) for 1 hour. All data are presented in fig. S5.

Preparation of LLPS-induced DOPA-modified TLC-M nanofiber coatings

To produce LLPS-induced coatings on flat substrates, the inside wall of microtubule or three-dimensional (3D) microfluidic device, DOPA-modified TLC-M solution was first concentrated to 2 mg/ml after purification and then dialyzed against the dialysate buffers [20 mM tris-HCl, 50 mM NaCl, and 0.5 mM EDTA (pH 5)] at 4°C for 1 hour to remove excess NaCl and imidazole and produce solution containing high density of liquid-like droplets. Then, we added 2 ml of dialyzed DOPA-modified TLC-M protein solutions (2 mg/ml) to entirely cover the surface of cut flat substrates inside each well of a 24-well plate or injected dialyzed DOPA-modified TLC-M protein solutions (2 mg/ml) into a microtubule. The samples were then incubated overnight at 4°C. A thin layer of nanofiber coatings could form on the substrates or the inside wall of microtubule. Data are presented in Fig. 4 (A to C) and fig. S8.

Microfluidic devices made of polydimethylsiloxane (PDMS) were fabricated in J.Z.'s lab at the State Key Laboratory of Supramolecular Structure and Materials of Jilin University. To prepare protein coatings inside a microfluidic device, a PDMS microfluidic device was compressed onto a glass slide surface and connected to a syringe (1 ml) using a Teflon pipeline. DOPA-modified TLC-M liquid-like droplet solution was slowly injected into the microfluidic device channel. After incubation overnight at 4°C, copious amounts of deionized water were applied to wash the microfluidic device channel to remove any loosely bound proteins. Data are presented in Fig. 4D.

To produce LLPS-induced coatings in buffers with different pH values or different ionic strengths, DOPA-modified TLC-M solution was first concentrated to 2 mg/ml after purification and then dialyzed against the dialysate buffers (20 mM tris-HCl, 50 mM NaCl, and 0.5 mM EDTA) with different pH values (3, 5, 7, 9, and 11) or dialysate buffers [20 mM tris-HCl and 0.5 mM EDTA (pH 5)] with different NaCl concentrations (0.05, 0.2, 0.5, and 1.0 M) at 4°C for 1 hour. Then, we placed the cut flat substrates inside a 24-well plate. Two milliliters of dialyzed DOPA-modified TLC-M protein solutions were then added to entirely cover the surface of substrates. The samples were then incubated overnight at 4°C. A thin layer of nanofiber coatings could form on the substrates. Data are presented in Fig. 2 (E to G).

CR stain and nitro blue tetrazolium stain assay

CR stain was used as an amyloid detection assay to confirm the amyloid features for amyloid-like proteins. DOPA-containing proteins can be specifically stained by nitro blue tetrazolium (NBT) in

glycinate solutions because they can catalyze redox-cycling reactions at an alkaline pH (29). The NBT assay was thus used to confirm the successful tyrosinase modification of TLC-M.

Sixty microliters of protein samples (50 µg/ml) were spotted onto Protran BA83 nitrocellulose membranes (Whatman) with a dot-blot manifold (Schleicher & Schuell Minifold-I Dot-Blot System). For the CR stain assay, the membranes spotted with proteins were immersed in 20 ml of 0.0025 (m/v %) CR solution at room temperature for 1 hour, then taken out and washed three times with copious amounts of deionized water, and incubated in deionized water overnight. For the NBT stain assay, the membranes spotted with proteins were incubated in 20 ml of freshly made NBT solution (0.6 mg/ml) in 2 M potassium glycinate buffer (pH 10.0) at room temperature in a dark place (covered with aluminum foil) for 30 min. The membranes were washed twice with 10 ml of 0.16 M sodium borate solution and soaked in another 20 ml of sodium borate solution overnight. Optical images of the stained samples were captured with a camera. Data are presented in fig. S1 (A and C).

To further characterize the amyloid features of the amyloid nanofiber coatings, we used polarized light microscopy to confirm the green birefringence feature of CR-stained samples. Specifically, 20 µl of dialyzed protein solution (2 mg/ml) was pipetted onto a glass coverslip. After incubation overnight at 4°C, the samples were dried at room temperature, followed by immersion into 1 ml of 0.0025 (m/v %) CR solution at room temperature for 1 hour and washed 10 times with deionized water to thoroughly remove the non-specifically bound CR dye. Last, the CR-stained samples were observed under an optical microscopy equipped with crossed polarizers (Leica M205 FA). Data are presented in fig. S1B.

ThT assay

Freshly purified protein solutions (200 µl) containing different concentrations (0.2, 0.5, 1, and 2 mg/ml) of protein monomers were added into 96-well flat clear bottom black PS tissue culture-treated microplates (3603, Corning) and incubated at 4 or 25°C. ThT buffer was then added at a final concentration of 20 µM. The signals were measured every 30 min by a BioTek Synergy H1 microplate reader using BioTek GEN5 software set at an excitation of 438 nm and emission of 495 nm with a 475-nm cutoff. The ThT fluorescence was normalized by $(F_i - F_0)/(F_{\max} - F_0)$, where F_i stands for ThT intensity (fluorescence arbitrary unit) of samples, F_0 is the ThT background intensity, and F_{\max} is the maximum ThT intensity of samples over the experiments. Data are presented in Fig. 2C and figs. S3C and S4B.

Turbidity measurement

To monitor the formation of liquid-like droplets in protein solutions containing different concentrations of monomers, turbidity of absorbance at 600 nm was applied as an indicator. TLC-M absorbance was negligible at 600 nm. The relative turbidity is defined as $\ln(T/T_0)$, where T and T_0 are the light transmittance with and without sample, respectively (2). Protein solutions were added into cuvette and measured on Spectramax M5 (Molecular Devices) at different time intervals. Data are presented in Fig. 2D and figs. S3A and S4C.

Quartz crystal microbalance with dissipation

Gold sensors were purchased from Biolin Scientific (QSX301) and cleaned according to the protocol before use (2). QCM-D experiments were carried out in a Q-Sense Omega Auto system

(Biolin Scientific) using two flow modules in parallel. Samples were introduced into the modules at a flow rate of 0.02 ml/min using a four-channel Ismatec ICP-N4 peristaltic pump. In QCM-D, changes in resonance frequency (ΔF) and dissipation (ΔD) of a quartz crystal are recorded to measure the amount and viscoelastic properties, respectively, of a material deposited on the sensor. The crystal is excited at its fundamental frequency, approximately 5 MHz, and changes can be observed at the fundamental ($n = 1$), as well as overtone frequencies ($n = 3, 5, 7, 9, \text{ and } 11$). Readings taken at the fundamental frequency are not usually used, as they are prone to artifacts from the sensor clamp.

Freshly purified TLC-M solutions containing different concentrations (0.2, 0.5, 1, and 2 mg/ml) of monomers were introduced into the modules at 4°C for liquid-like droplets and 25°C for unaggregated monomers and nanofibers. The adsorbed proteins on the gold sensors were then washed with deionized water for 20 min to remove any nonspecifically bound materials. Data are presented in Figs. 2G and 3D and figs. S3B and S6.

BCA assay

To confirm the role of gravity on adsorption of liquid-like coacervates toward a given substrate, a BCA assay was applied to quantify the amount of liquid-like droplets adsorbed on the substrate. Specifically, glass substrates ($R = 5$ mm) sitting at the bottom (bottom surface) or floating on the solution surface (upper surface) in TLC-M solutions with different concentrations (0.2, 0.5, 1, and 2 mg/ml) were taken out at different time intervals. Glass substrates were treated with formic acid for 12 hours, and the treated solution was then freeze-dried. Then, collected protein samples from the glass substrates were redissolved in 500 μ l of PBS. BCA reagent buffer (A:B, 50:1) was mixed with protein solutions at 8:1 and incubated at 37°C for 30 min. Each sample (200 μ l) was added into a 96-well plate, and the absorption was measured at 562 nm. Diluted albumin (bovine serum albumin) solutions were applied as concentration standards. Data are presented in table S1.

Underwater adhesion force measurements

The AFM colloidal probe technique (29) was used for adhesion force and adhesion energy measurements. This technique is based on quantification of the adhesion interactions between adhesive material (preabsorbed on a planar mica surface in the experiments) and a colloidal sphere (with well-defined size). It essentially measures the asymmetric adhesion of materials, which prebind firmly to mica and bind temporarily to the AFM tip surface during measurement. We used the continuous measurement mode in our experiments. The continuous measurement mode enabled us to assess the cyclic behaviors of contacts between materials and AFM tip surfaces.

AFM force measurements were carried out at room temperature in buffered solutions [20 mM tris-HCl and 50 mM NaCl (pH 5 for tyrosinase-modified protein or pH 7 for unmodified protein)] using an Asylum MFP-3D AFM (Asylum Research). Force measurements (force-displacement curves) were made at a rate of 1 Hz, using Si_3N_4 or Si cantilevers modified with a silica sphere coated with gold layers with a radius of 10 μ m and calibrated spring constants of 8.9 N/m (NovaScan). Image processing and analysis of force curves were performed using Igor Pro (WaveMetrics) data analysis software and Origin 8.0 software (OriginLab Corporation). We used continuous measurement mode for each type of adhesive material tested. Data from adhesion tests at five spots (each spot with

a total of five continuous measurements) were used for statistical assessments in this study.

For each measurement, we also applied control tests by directly measuring adhesion on a clean mica surface under the same conditions. These procedures thus ensured that all the presented force curves were measured on real samples rather than contaminated surfaces. Typical force curves measured on a clean mica surface (as a negative control) are shown in fig. S7C. Cooler heater module and BioHeater module were applied to control solution temperature for adhesion performance assessment at varied temperature.

Last, measured adhesion forces, F_{ad} , taken at the point of maximum force on the retraction curves, were related to the adhesion energy per area (E_{ad}) according to the Johnson-Kendall-Roberts (29) theory for deformable surfaces.

For a similar sphere/sphere system

$$F_{\text{ad}} = 1.5\pi RE_{\text{ad}}$$

For a dissimilar sphere/flat system, which is the case in our study

$$F_{\text{ad}} = 3\pi RE_{\text{ad}}$$

where R is the radius of contact.

The reported forces and adhesion energies in this paper are given as absolute values. Data are presented in Fig. 3 (B, C, F, and G) and fig. S7 (A and B). Note that, except those specifically noted adhesion measurements that were carried out at different temperatures, all the adhesion measurements by an AFM colloidal probe were carried out in aqueous solution at 25°C.

Synthesis of CdSeS@ZnS QDs

$\text{Cd}(\text{OAc})_2$ reacted with S and Se at 150°C to form CdSeS core, followed by addition of $\text{Zn}(\text{OAc})_2$ and S, and heated at 270°C to form the ZnS shell to produce the CdSeS@ZnS QDs. Product was stored in hexane. One milliliter of QD solution was added to 1 ml of HS-NTA in methane solution (pH was tuned to 12) and then vortexed for 5 min. The precipitate was dispersed in 10 ml of PBS solution after centrifugation. The aqueous layer was filtered with 0.2- μ m Acrodisc syringe filters (Pall). Twenty microliters of 50 mM CoCl_2 solution was added to 10 ml of HS-NTA decorated QDs in PBS solution. Then, the solution was vortexed, centrifuged at 5000 rpm for 3 min, and filtered with 0.2- μ m Acrodisc syringe filters (Pall). The samples thusly prepared were stored in dark place at 4°C.

Adsorption of QDs onto adhesive coatings

To visualize the protein coatings formed on substrates and along the inside wall of channel, a solution containing red QDs was carefully injected into the channel and incubated for 1 hour and thoroughly washed with deionized water to remove the loosely bound QDs. Photographs were taken under UV light (254 nm). The adsorption of QDs onto protein coatings was based on metal coordination chemistry between His-tags and Ni-NTA-decorated QDs. Coating images were captured using camera (Canon EOS-3), and 3D images were recorded using a confocal microscope. Data are presented in Figs. 2A and 4 (A, C, and D) and fig. S8B.

Application demonstration of damage repairs

A groove (500- μ m width and 200- μ m depth) on a Teflon surface was purposely created by scraping the substrate using a blade. To repair the damage, syringes containing DOPA-modified TLC-M solution

containing liquid-like droplets (2 mg/ml) and fluorescent PS microspheres (10 μm in diameter) solution (10 mg/ml) 1:1 were simultaneously coinjected around the damage sites along the groove. The repaired samples were then incubated overnight at 4°C to ensure full curing and were later on inspected under SEM after drying in air. Data are presented in Fig. 4F.

Contact angle measurements

The contact angle measurements were performed with deionized water (2 μl) at room temperature (41) using a SL200KS contact angle meter (Kino) following the sessile drop method. Nanofiber coatings on diverse substrates were thoroughly washed with deionized water and dried with nitrogen gas. Samples were then placed on the analysis plane of the contact angle analyzer. The results were analyzed using One Attension software, and the drop shape was fitted using Young-Laplace method. The substrates without coatings were used as control. Data are presented in fig. S8C.

X-ray fiber diffraction of amyloid nanofibers

Amyloid nanofiber coatings formed by TLC-M at 4 or 25°C were scraped and resuspended in deionized water. Mature nanofibers formed by TDP43 LC were pelleted by centrifugation at 10,000g, followed by washing several times with copious amounts of deionized water to remove remaining salts. The nanofiber pellets were then suspended in deionized water. Two microliters of suspensions were pipetted between two fire-polished glass rods and dried for several hours. The diffraction data were collected on a Rigaku MicroMax 007 x-ray generator and an R-AXIS IV++ area detector. Data are presented in Fig. 2A and fig. S4A.

TEM imaging

Detailed procedures for sample preparation for TEM imaging are described below: 10 μl of protein solution containing liquid-like droplets or nanofibers was directly deposited on a piece of carbon film-supported 400-mesh copper grid (Beijing Zhongjingkeyi Technology Co. Ltd.) for 10 min. Excessive solution was then quickly wicked away with pieces of filter paper and washed three times with 10 μl of deionized water. Samples were negatively stained with 10 μl of 2 wt % uranyl acetate right away and then dried under an infrared lamp for 20 min. All TEM images were collected on a Tecnai G2 F20 TEM operated at a 120-kV accelerating voltage. Data are presented in Fig. 2B and fig. S2 (B and C).

AFM imaging

Typically, for sample preparation for AFM imaging, 200 μl of protein solution containing assembled structures was incubated on a mica surface for 30 min to allow sample deposition on mica surface. The excessive solution was then washed away twice with 200 ml of deionized water. The mica surface was dried through a constant flow of nitrogen gas and then immediately collected for AFM imaging. Tapping mode AFM was performed on an Asylum MFP-3D AFM (Asylum Research) using microcantilevers ($k = 26.1 \text{ N/m}$ and $V = \sim 300 \text{ kHz}$). Data are presented in Fig. 2B and fig. S2A.

SEM imaging

For sample preparation for SEM analysis, the protein coatings formed on a Teflon plate were washed with deionized water and dried under constant flow of nitrogen gas. To image the interface formed between protein coatings and Teflon plate, the sample was

cut vertically using a blade. The cross section of the sample was then imaged using SEM. SEM images were taken using a JSM 7800 SEM operated at a 5-kV accelerating voltage. Data are presented in Fig. 4 (B and F) and fig. S8A.

DIC microscopy and confocal fluorescence microscopy imaging

Five microliters of protein solution containing liquid-like droplets or nanofibers was dropped on a piece of clean glass slide ($1.0 \pm 0.2 \text{ mm}$ in thickness; Citoglas) and then covered by a piece of cover glass (0.13 to 0.16 mm; microscopic cover glass, Citoglas). DIC imaging was performed on a ZEISS Z2 microscope equipped with AxioCam 506 camera (ZEISS). The 3D confocal images of microfluidic channel or microtubule were obtained with a Leica TCS SP8 confocal microscope. The 561-nm laser was used for excitation of QDs. Data are presented in Figs. 2F and 4 (C and D).

X-ray photoelectron spectroscopy

Bare substrate (Teflon or glass) and protein nanofiber-coated substrate (Teflon or glass) were both used for XPS analysis. XPS was conducted using an ESCALAB 250Xi (Thermo Fisher Scientific) with a monochromatic Al-K α line (1486.6 eV). Elements of samples surfaces were measured at a step width of 0.01 eV. Data are presented in Fig. 4B.

Statistical analysis

Data analysis was performed on Origin 9 software and expressed as means \pm SD, unless otherwise specified. Statistical comparisons between two groups were based on Student's paired t test with two-tailed distribution. A value of $P < 0.01$ was considered to be statistically significant.

SUPPLEMENTARY MATERIALS

Supplementary material for this article is available at <http://advances.sciencemag.org/cgi/content/full/5/8/eaax3155/DC1>

Fig. S1. CR and NBT staining of self-assembled amyloid nanofibers.

Fig. S2. Morphology of self-assembled amyloid nanofibers and phase separated liquid-like droplets of TLC-M.

Fig. S3. Protein concentration effect on kinetics of liquid-like droplet settling and amyloid assembly.

Fig. S4. X-ray fiber diffraction, ThT fluorescence curves, and turbidity-time curves of TDP43 LC.

Fig. S5. 3D histogram showing specific parameters that influence the formation of liquid-like droplets.

Fig. S6. Frequency change comparison and ΔF - ΔD curves for different protein samples tested in QCM-D experiments.

Fig. S7. Force-distance curve tested by colloidal probe AFM.

Fig. S8. LLPS-driven DOPA-modified TLC-M coatings on diverse of substrates.

Table S1. Gravity effect on coacervate adsorption toward a given surface.

REFERENCES AND NOTES

- R. J. Stewart, C. S. Wang, H. Shao, Complex coacervates as a foundation for synthetic underwater adhesives. *Adv. Colloid Interface Sci.* **167**, 85–93 (2011).
- W. Wei, Y. Tan, N. R. Martinez Rodriguez, J. Yu, J. N. Israelachvili, J. H. Waite, A mussel-derived one component adhesive coacervate. *Acta Biomater.* **10**, 1663–1670 (2014).
- I. Kaminker, W. Wei, A. M. Schrader, Y. Talmon, M. T. Valentine, J. N. Israelachvili, J. H. Waite, S. Han, Simple peptide coacervates adapted for rapid pressure-sensitive wet adhesion. *Soft Matter* **13**, 9122–9131 (2017).
- D. S. Hwang, Y. Gim, H. J. Yoo, H. J. Cha, Practical recombinant hybrid mussel bioadhesive fp-151. *Biomaterials* **28**, 3560–3568 (2007).
- W. Wei, L. Petrone, Y. Tan, H. Cai, J. N. Israelachvili, A. Miserez, J. H. Waite, An underwater surface-drying peptide inspired by a mussel adhesive protein. *Adv. Funct. Mater.* **26**, 3496–3507 (2016).
- J. Wang, T. Scheibel, Coacervation of the recombinant *Mytilus galloprovincialis* foot protein-3b. *Biomacromolecules* **19**, 3612–3619 (2018).
- S. Kim, J. Huang, Y. Lee, S. Dutta, H. Y. Yoo, Y. M. Jung, Y. Jho, H. Zeng, D. S. Hwang, Complexation and coacervation of like-charged polyelectrolytes inspired by mussels. *Proc. Natl. Acad. Sci. U.S.A.* **113**, E847–E853 (2016).

8. S. Kim, H. Y. Yoo, J. Huang, Y. Lee, S. Park, Y. Park, S. Jin, Y. M. Jung, H. Zeng, D. S. Hwang, Y. Jho, Salt triggers the simple coacervation of an underwater adhesive when cations meet aromatic π electrons in seawater. *ACS Nano* **11**, 6764–6772 (2017).
9. B. Yang, S. Jin, Y. Park, Y. M. Jung, H. J. Cha, Coacervation of interfacial adhesive proteins for initial mussel adhesion to a wet surface. *Small* **14**, e1803377 (2018).
10. S. F. Banani, H. O. Lee, A. A. Hyman, M. K. Rosen, Biomolecular condensates: Organizers of cellular biochemistry. *Nat. Rev. Mol. Cell Biol.* **18**, 285–298 (2017).
11. J. B. Woodruff, A. A. Hyman, E. Boke, Organization and function of non-dynamic biomolecular condensates. *Trends Biochem. Sci.* **43**, 81–94 (2018).
12. Y. Shin, C. P. Brangwynne, Liquid phase condensation in cell physiology and disease. *Science* **357**, eaaf4382 (2017).
13. J. B. Woodruff, B. F. Gomes, P. O. Widlund, J. Mahamid, A. Honigsmann, A. A. Hyman, The centrosome is a selective condensate that nucleates microtubules by concentrating tubulin. *Cell* **169**, 1066–1077.e10 (2017).
14. E. Boke, M. Ruer, M. Wüthrich, M. Coughlin, R. Lemaître, S. P. Gygi, S. Alberti, D. Drechsel, A. A. Hyman, T. J. Mitchison, Amyloid-like self-assembly of a cellular compartment. *Cell* **166**, 637–650 (2016).
15. T. E. Audas, D. E. Audas, M. D. Jacob, J. D. Ho, M. Khacho, M. Wang, J. K. Perera, C. Gardiner, C. A. Bennett, T. Head, O. N. Kryvenko, M. Jorda, S. Daunert, A. Malhotra, L. Trinkle-Mulcahy, M. L. Gonzalgo, S. Lee, Adaptation to stressors by systemic protein amyloidogenesis. *Dev. Cell* **39**, 155–168 (2016).
16. C. P. Brangwynne, P. Tompa, R. V. Pappu, Polymer physics of intracellular phase transitions. *Nat. Phys.* **11**, 899–904 (2015).
17. A. Molliex, J. Temirov, J. Lee, M. Coughlin, A. P. Kanagaraj, H. J. Kim, T. Mittag, J. P. Taylor, Phase separation by low complexity domains promotes stress granule assembly and drives pathological fibrillization. *Cell* **163**, 123–133 (2015).
18. L.-P. Bergeron-Sandoval, N. Safaei, S. W. Michnick, Mechanisms and consequences of macromolecular phase separation. *Cell* **165**, 1067–1079 (2016).
19. H. Wu, M. Fuxreiter, The structure and dynamics of higher-order assemblies: Amyloids, signalosomes, and granules. *Cell* **165**, 1055–1066 (2016).
20. J. Berry, C. P. Brangwynne, M. Haataja, Physical principles of intracellular organization via active and passive phase transitions. *Rep. Prog. Phys.* **81**, 046601 (2018).
21. M. Kato, T. W. Han, S. Xie, K. Shi, X. Du, L. C. Wu, H. Mirzaei, E. J. Goldsmith, J. Longgood, J. Pei, N. V. Grishin, D. E. Frantz, J. W. Schneider, S. Chen, L. Li, M. R. Sawaya, D. Eisenberg, R. Tycko, S. L. McKnight, Cell-free formation of RNA granules: Low complexity sequence domains form dynamic fibers within hydrogels. *Cell* **149**, 753–767 (2012).
22. E. W. Danner, Y. Kan, M. U. Hammer, J. N. Israelachvili, J. H. Waite, Adhesion of mussel foot protein Mefp-5 to mica: An underwater superglue. *Biochemistry* **51**, 6511–6518 (2012).
23. A. E. Conicella, G. H. Zerze, J. Mittal, N. L. Fawzi, ALS mutations disrupt phase separation mediated by α -helical structure in the TDP-43 low-complexity C-terminal domain. *Structure* **24**, 1537–1549 (2016).
24. H.-R. Li, T.-C. Chen, C.-L. Hsiao, L. Shi, C.-Y. Chou, J.-r. Huang, The physical forces mediating self-association and phase-separation in the C-terminal domain of TDP-43. *Biochim. Biophys. Acta Proteins Proteom.* **1866**, 214–223 (2018).
25. T. W. Han, M. Kato, S. Xie, L. C. Wu, H. Mirzaei, J. Pei, M. Chen, Y. Xie, J. Allen, G. Xiao, S. L. McKnight, Cell-free formation of RNA granules: Bound RNAs identify features and components of cellular assemblies. *Cell* **149**, 768–779 (2012).
26. Y. Lin, D. S. W. Protter, M. K. Rosen, R. Parker, Formation and maturation of phase-separated liquid droplets by RNA-binding proteins. *Mol. Cell* **60**, 208–219 (2015).
27. C. P. Brangwynne, C. R. Eckmann, D. S. Courson, A. Rybarska, C. Hoeg, J. Gharakhani, F. Jülicher, A. A. Hyman, Germline P granules are liquid droplets that localize by controlled dissolution/condensation. *Science* **324**, 1729–1732 (2009).
28. C. S. Wang, R. J. Stewart, Localization of the bioadhesive precursors of the sandcastle worm, *Phragmatopoma californica* (Fewkes). *J. Exp. Biol.* **215**, 351–361 (2012).
29. C. Zhong, T. Gurry, A. A. Cheng, J. Downey, Z. Deng, C. M. Stultz, T. K. Lu, Strong underwater adhesives made by self-assembling multi-protein nanofibres. *Nat. Nanotechnol.* **9**, 858–866 (2014).
30. C. R. So, K. P. Fears, D. H. Leary, J. M. Scancell, Z. Wang, J. L. Liu, B. Orihuela, D. Rittschof, C. M. Spillmann, K. J. Wahl, Sequence basis of barnacle cement nanostructure is defined by proteins with silk homology. *Sci. Rep.* **6**, 36219 (2016).
31. K. P. Fears, B. Orihuela, D. Rittschof, K. J. Wahl, Acorn barnacles secrete phase-separating fluid to clear surfaces ahead of cement deposition. *Adv. Sci.* **5**, 1700762 (2018).
32. B. An, X. Wang, M. Cui, X. Gui, X. Mao, Y. Liu, K. Li, C. Chu, J. Pu, S. Ren, Y. Wang, G. Zhong, T. K. Lu, C. Liu, C. Zhong, Diverse supramolecular nanofiber networks assembled by functional low-complexity domains. *ACS Nano* **11**, 6985–6995 (2017).
33. M. Cui, Q. Qi, T. Gurry, T. Zhao, B. An, J. Pu, X. Gui, A. A. Cheng, S. Zhang, D. Xun, M. Becce, F. Briatico-Vangosa, C. Liu, T. K. Lu, C. Zhong, Modular genetic design of multi-domain functional amyloids: Insights into self-assembly and functional properties. *Chem. Sci.* **10**, 4004–4014 (2019).
34. D. S. Hwang, J. H. Waite, M. Tirrell, Promotion of osteoblast proliferation on complex coacervation-based hyaluronic acid–recombinant mussel adhesive protein coatings on titanium. *Biomaterials* **31**, 1080–1084 (2010).
35. D. Priftis, M. Tirrell, Phase behaviour and complex coacervation of aqueous polypeptide solutions. *Soft Matter* **8**, 9396–9405 (2012).
36. H. Jiang, S. Wang, Y. Huang, X. He, H. Cui, X. Zhu, Y. Zheng, Phase transition of spindle-associated protein regulate spindle apparatus assembly. *Cell* **163**, 108–122 (2015).
37. T. M. Franzmann, M. Jahnel, A. Pozniakovskiy, J. Mahamid, A. S. Holehouse, E. Nüske, D. Richter, W. Baumeister, S. W. Grill, R. V. Pappu, A. A. Hyman, S. Alberti, Phase separation of a yeast prion protein promotes cellular fitness. *Science* **359**, eaao5654 (2018).
38. J. R. Simon, N. J. Carroll, M. Rubinstein, A. Chilkoti, G. P. López, Programming molecular self-assembly of intrinsically disordered proteins containing sequences of low complexity. *Nat. Chem.* **9**, 509–515 (2017).
39. E. M. Langdon, Y. Qiu, A. Ghanbari Niaki, G. A. McLaughlin, C. A. Weidmann, T. M. Gerbich, J. A. Smith, J. M. Crutchley, C. M. Termini, K. M. Weeks, S. Myong, A. S. Gladfelter, mRNA structure determines specificity of a polyQ-driven phase separation. *Science* **360**, 922–927 (2018).
40. E. W. Martin, T. Mittag, Relationship of sequence and phase separation in protein low-complexity regions. *Biochemistry* **57**, 2478–2487 (2018).
41. X. Wang, J. Pu, B. An, Y. Li, Y. Shang, Z. Ning, Y. Liu, F. Ba, J. Zhang, C. Zhong, Programming cells for dynamic assembly of inorganic nano-objects with spatiotemporal control. *Adv. Mater.* **30**, e1705968 (2018).

Acknowledgments: We thank S. L. McKnight and M. Kato (University of Texas, Southwestern Medical Center) for the gift of the pHIS-parallel1 vector, W. Jiang for providing the basic training on molecular cloning, X. Wang for AFM training, Y. Shang for XPS characterization, undergraduate students D. Xun and L. Kong for protein expression, and technician M. Xin for text proofreading. AFM characterization and QCM-D measurement were executed at the Analytical Instrumentation Center (AIC), and SEM and TEM characterization were performed at the Center for High-resolution Electron Microscopy (CHEM) at the School of Physical Science and Technology (SPST), ShanghaiTech University. **Funding:** This work was partially sponsored by the National Natural Science Foundation of China (grant no. 31570972) and the Open Financial Fund of the Qingdao National Laboratory for Marine Science and Technology (grant no. QNLM2016ORP0403). C. Zhong also acknowledges start-up funding support from ShanghaiTech University and 1000 Youth Talents Program, granted by the Chinese Central Government. **Author contributions:** C.Zho. directed the research. C.Zho. and M.C. conceived the idea and designed the research. M.C. carried out or participated in all the experiments. X.W. synthesized QDs and performed TEM. B.A. generated the genetic constructs. C.Zha. performed SEM. X.G. and C.L. carried out the polarized light microscopic imaging, confocal fluorescence microscopic imaging, and the x-ray fiber diffraction experiment. K.L. and Y.L. performed coating on diverse of substrates. P.G. and J.Z. fabricated microfluidic devices. C.Zho. and M.C. analyzed the data, discussed the results, and wrote the manuscript with help from all authors. **Competing interests:** M.C. and C.Zho. are inventors on a patent application related to this work filed by ShanghaiTech University (no. PCT/CN2018/101219, filed 18 August 2018). The authors declare that they have no other competing interests. **Data and materials availability:** All data needed to evaluate the conclusions in the paper are present in the paper and/or the Supplementary Materials. Additional data related to this paper, including but not limited to amino acid sequences, genetic designs, and gene sequences for all genetic constructs, may be requested from the authors.

Submitted 13 March 2019

Accepted 16 July 2019

Published 23 August 2019

10.1126/sciadv.aax3155

Citation: M. Cui, X. Wang, B. An, C. Zhang, X. Gui, K. Li, Y. Li, P. Ge, J. Zhang, C. Liu, C. Zhong, Exploiting mammalian low-complexity domains for liquid-liquid phase separation–driven underwater adhesive coatings. *Sci. Adv.* **5**, eaax3155 (2019).

Exploiting mammalian low-complexity domains for liquid-liquid phase separation–driven underwater adhesive coatings

Mengkui Cui, Xinyu Wang, Bolin An, Chen Zhang, Xinrui Gui, Ke Li, Yingfeng Li, Peng Ge, Junhu Zhang, Cong Liu and Chao Zhong

Sci Adv 5 (8), eaax3155.
DOI: 10.1126/sciadv.aax3155

ARTICLE TOOLS

<http://advances.sciencemag.org/content/5/8/eaax3155>

SUPPLEMENTARY MATERIALS

<http://advances.sciencemag.org/content/suppl/2019/08/19/5.8.eaax3155.DC1>

REFERENCES

This article cites 41 articles, 6 of which you can access for free
<http://advances.sciencemag.org/content/5/8/eaax3155#BIBL>

PERMISSIONS

<http://www.sciencemag.org/help/reprints-and-permissions>

Use of this article is subject to the [Terms of Service](#)

Science Advances (ISSN 2375-2548) is published by the American Association for the Advancement of Science, 1200 New York Avenue NW, Washington, DC 20005. 2017 © The Authors, some rights reserved; exclusive licensee American Association for the Advancement of Science. No claim to original U.S. Government Works. The title *Science Advances* is a registered trademark of AAAS.